Check for updates

Enhanced separation of europium radionuclides from active solutions using a novel sorbent of gadolinium metal–organic framework

Mohamed A. Hamouda, [ID] *[a] Reda R. Sheha,[b] Said M. El-Sheikh, [ID] *[c] A. T. Kandil,[a] Omnia I. Ali [ID] [a] and Sheta M. Sheta [ID] *[d]

Preserving environmental quality when disposing of hazardous waste, especially radioactive waste, is a relevant research area that attracts the interest of global scientists. The separation of harmful species on the surface of novel adsorbent metal–organic frameworks (MOFs) is a promising and effective method for achieving this goal. This study identifies a new metal–organic framework known as melamine–terephthalic acid (MTGd MOF) that was synthesized and then treated with oxalic acid to produce modified MTGd–OX MOF that has been characterized. The MOFs were formed successfully based on the characterization results. BET results show that MTGd MOF and MTGd–OX MOF have surface areas of 1857.40 and 1955.16 m^2 g^{-1}, respectively. The prepared materials were used in batch studies to explore the sorption behavior of Eu radionuclides onto unmodified and modified MOFs. The results indicate that MTGd–OX MOF had a more effective sorption capacity than MTGd MOF. Several variables, including the pH, ionic strength, initial concentration of $^{152+154}$Eu ions, contact time, and optimal conditions for separating $^{152+154}$Eu onto MTGd–OX MOF, were examined, including temperature. The MTGd–OX MOF capacity is about 37.22 mg g^{-1} at pH 3.5, and the equilibrium was reached after 4 hours. The efficiency of MTGd–OX MOF as a sorbent was assessed by analyzing a real waste sample, which showed it had significant sorption efficiency.

Introduction

The application of nuclear technology in many industries has led to the production of significant amounts of hazardous radioactive waste, which poses a risk to the quality of the environment and public health. Radioactive wastes are produced from many sources, such as nuclear power generation, and used in a variety of industries, research fields, and agricultural and medical sectors.[1,2] The unique properties of long-lived radioactive elements pose serious environmental risks. Consequently, these radioisotopes are considered to be the most detrimental to ecosystems. Their persistence in the environment and potential to accumulate in living organisms pose significant risks to both ecosystems and human health.[3]

Previously, various technologies have been developed to remove radioactive materials from wastewater, including ion exchange, liquid–liquid separation, adsorption, and precipitation. Among them, ion exchange is widely used in the treatment of nuclear wastewater due to its high selectivity, simplicity, and reliability. Liquid-to-liquid extraction plays an important role in nuclear fuel reprocessing and actinide recovery. At the same time, chemical precipitation remains a traditional and effective method for removing large amounts of radioactive substances, especially radioactive liquid waste, at the primary treatment stage.[4] The utilization of such methods is infrequent, primarily, and yields dangerous intermediates that are not self-cleaning or regenerable.[5] Conversely, adsorption offers several advantages, such as cost, convenience in usage, simplicity, and regeneration.[6–8] Numerous sorbents, including activated carbon, zeolites, and chitosan-based materials, have been examined for their potential to remove radionuclides from aqueous systems. Applications encompass laboratory-scale bulk investigations and tests conducted with actual radioactive waste solutions.[9–11]

Materials that combine metal ions or clusters with organic linkers to generate hybrid structures are known as MOFs. This combination produces materials with distinctive and appealing attributes. MOFs offer the following advantages for adsorption: high surface area provides sufficient active sites, pore size can be engineered to match the target molecules selectively, chemical functionalization enhances specificity, chemical stability under different conditions, selectivity in substance

[a]Department of Chemistry, Faculty of Science, Helwan University, Cairo, 11795, Egypt. E-mail: mohammadatya95@gmail.com

[b]Nuclear Chem. Dept., Hot Lab Center, Egyptian Atomic Energy Authority, P. O. 13759, Cairo, Egypt

[c]Department of Nanomaterials and Nanotechnology, Central Metallurgical R & D Institute, Cairo, 11421, Egypt. E-mail: selsheikh2001@gmail.com; Tel: +20-1022316076

[d]Department of Inorganic Chemistry, National Research Centre, Cairo, 12622, Egypt. E-mail: dr.sheta.nrc@gmail.com; Fax: +20-02-33370931; Tel: +20-1009697356

favouring, regeneration ability for more usage, cost-efficient and recyclable, green synthesis methodology in line with green chemistry, applicability in environmental, storage and separations.[12] Thus, MOFs are attractive options for the removal of radioactive ions from liquid wastes because of their unique characteristics. Recently, MOFs were effectively applied to regulate pollution by removing hazardous and radioisotopes from the environment.[4,13–15]

MOFs exhibit a diverse range of properties owing to the presence of organic linkers, porosity, and metal ions or clusters. Modification of MOFs with the functionalizing agents is a great and practical way to improve stability, flexibility, porosity, and crystallization.[14,16,17] As an instance, the MIL-101 MOF functionalized with amino, EDTA, and carboxyl groups enhanced the removal efficiency of UO_2^{2+} ions.[18] Moreover, Th^{4+} ions were eliminated using UiO-66, UiO-66-$(COOH)_2$, and their carboxyl derivatives. Zhang. *et al.* found that UiO-66's capacity to absorb Th^{4+} was significantly increased when carboxyl groups were added.[19,20] The bi-ligand synthesis approach enhances the MOF's properties, such as size, shape, and morphology.

MOFs with diverse properties can be crafted by utilizing specific ligands with networks that focus on coordination bonds, offering greater structural stability when compared to hydrogen-bonded structures. Moreover, the combination of stiff carboxylic acid bonds and cations such as Cu^{2+}, Zn^{2+}, Co^{2+}, Ni^{2+}, *etc.* might have a role in the instability of several MOF structures. Therefore, coordination bonds formed from soft metallic ions and softer nitrogen-containing organic bonding are stronger than coordination bonds formed by strong carboxylic acid linkages.[21,22] A recent theoretical study has highlighted those ligands featuring amide linkages with nitrogen and oxygen have emerged as a focal point in actinide and lanthanide removal research. These ligands demonstrate favourable extraction and separation properties, incorporating both soft and hard electron donors, along with the advantage of scalable production.[23] For example, ZIFs (Zeolitic Imidazolate Frameworks) have superior chemical and heat stability, owing to their soft–soft coordination between divalent metal ions (*e.g.*, Zn^{2+} or Co^{2+}) and nitrogen-based imidazolate linkers, resulting in more stable and hydrolytically stable bonds than in hard acid–base coordination found in carboxylate-linked MOFs. This stability renders ZIFs exceptionally effective towards the removal of radionuclides such as uranium (UO_2^{2+}), iodine ($^{129}I^-$, $^{131}I^-$, I_2), and noble gases (Xe, Kr).[24] In addition, nitrogen-rich ligands (such as 1,2,4-triazines, BTBPs, and BTPhens) are key to achieving selectivity in the context of Pearson's theory of hard and soft acids and bases (HSAB), especially for the separation of f-group elements, especially Am(III), Eu(III) and Cm(III), and recent advances in the design of hydrophilic linkers have highlighted this importance. By forming more covalent and acid-resistant coordination with the soft actinoids, ligands with lighter nitrogen donor atoms improve the separation efficiency compared to the harder lanthanide cations. This approach optimizes ligand structure–function correlations to maximize stability, selectivity, and industrial applicability, reducing organic solvent consumption and improving the sustainability of aqueous reprocessing.[25] In this regard, our research group

developed strontium bi-ligand MOF based on terephthalic acid and melamine (MTSr MOF), which has been applied to eliminate radionuclides $^{152+154}Eu$.[26] On the other hand, the sorption capacity of this MOF is low. Thus, a modified version of the MTSr MOF using oxalic acid was proposed as the MTSr–OX MOF to regulate the size, shape, and sorption behaviours of $^{152+154}Eu$ radionuclides.[16] A gadolinium bi-ligand MOF was synthesized, characterized, and employed to extract $^{152+154}Eu$ from active water. The main goal of gadolinium is to evaluate how metal ion hardness, coordination geometry, and bond compatibility affect the stability and removal efficiency of the bi-ligand MOFs under radiochemical conditions, an important consideration for future designs aimed at radioactive f-block separation. The influence of several factors on the sorption of $^{152+154}Eu$ will be investigated. Additionally, an investigation will be conducted into the isotherms, kinetics, thermodynamics, and possible mechanisms of $^{152+154}Eu$ separation using the produced MOF.

Results and discussion

MTGd MOF characterization

SEM/EDX and TEM. Fig. 1 represents the FE-SEM images of MTGd MOF and MTGd–OX MOF. FE-SEM images show the particles morphology and size. These particles are coalesced to form agglomerates in the form of cubic, rod, and platelet-like shapes, as shown in (Fig. 1a and b). Whereas (Fig. 1c and d) demonstrates the FE-SEM images of the MTGd–OX MOF with two magnifications. The images indicated that the MTGd–OX MOF has hexagonal rods bounded by six long rectangular faces with sharp edges. The hexagonal rods have a width of 0.08–0.33 μm and a length of 0.20–0.60 μm with an aspect ratio of 0.4–0.55. The mapping analysis of MTGd MOF indicates the existence of O, N, C, Cl, and Gd, which serve as the building blocks.

Fig. 2a shows coloured constituent maps using a single-point analysis. Individual mappings regarding all the components are
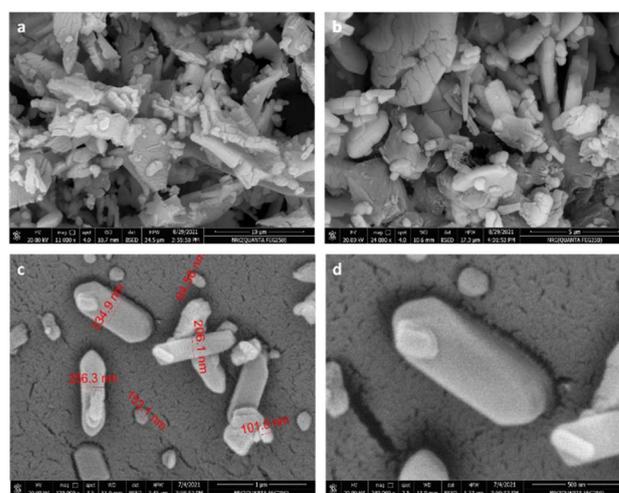

Fig. 1 Field-emission scanning electron microscopy images of MTGd MOF (a and b), and MTGd–OX MOF (c and d) at different magnifications.
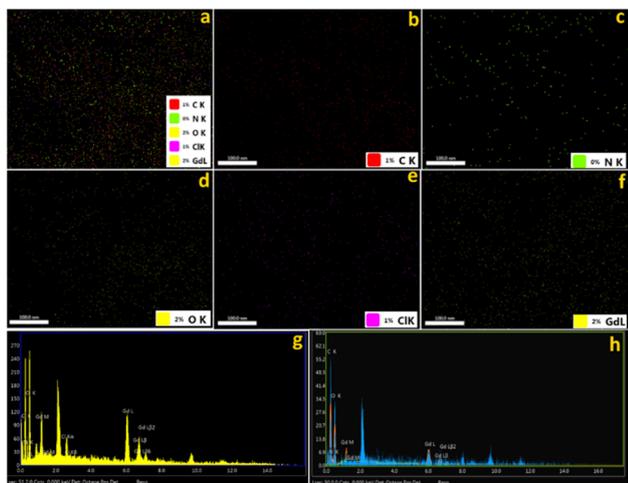
Fig. 2 Energy-dispersive X-ray analysis with a single point EDX mapping analysis of MTGd MOF (a–g), and MTGd–OX MOF (h).

illustrated in (Fig. 2b–f). The SEM-EDX analysis of MTGd MOF (Fig. 2g) and MTGd–OX MOF (Fig. 2h) revealed the presence of oxygen, nitrogen, carbon, and gadolinium.

The data obtained confirm the successful modification of MTGd–OX MOF. TEM images of MTGd MOF and MTGd–OX MOF are shown in (Fig. 3a–c), and (Fig. 3d–f), respectively. MTGd–OX MOF revealed rod-like crystals, while MTGd MOF displayed rectangular disk-like morphology with rounded corners and a smooth surface with about 60–300 nm, which is in good agreement with FE-SEM images. MTGd–OX MOF had a more regular shape and higher crystallinity compared to unmodified MOF.

FT-IR spectra

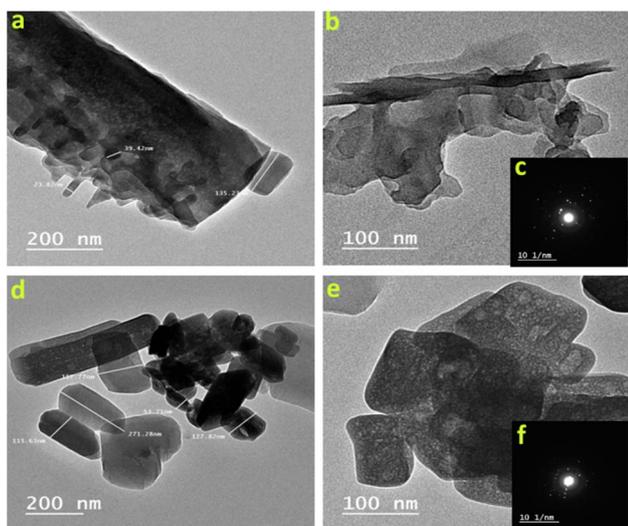Fig. S1 displays the FTIR spectra for both the unmodified and modified MOFs. In MTGd and MTGd–OX MOFs, peaks at 3373

Fig. 3 The transmission electron microscopy images (TEM) (a and b) and SAED (c) of MTGd MOF, and (TEM) (d and e) and SAED (f) of MTGd–OX MOF.

and 3216 cm^{-1} were assigned to the N–H stretching frequency of the melamine ligand. These peaks showed a shift from the pure melamine, which appeared at 3417 and 3323 cm^{-1}, respectively.[27] In MTGd MOF, the peak at 3058 cm^{-1} indicated the stretching vibrational C–H bond in the terephthalic acid ligand, which was shifted to 3094 cm^{-1} in MTGd–OX MOF. This can be due to hydrogen bonding between the C–H bond and oxalic acid carboxylic groups during modification.[28–30] The peak at 2823 cm^{-1} in the modified MOF was associated with the bending O–H bond.[29] A less intense band at 1655 cm^{-1} in MTGd MOF revealed the appearance of the carbonyl group C=O. This can be attributed to the formation of an amide group rather than the benzene dicarboxylic acid C=O peak, which appeared at 1690 cm^{-1}.[31,32] The carbonyl group in MTGd–OX MOF shows a strong peak near 1616 cm^{-1}, confirming the presence of oxalic acid after the modification. In both MOFs, the peaks revealed at 1585 and 1502 cm^{-1} indicated the C=C aromatic of the terephthalic acid ligand, whereas the peak at 1539 cm^{-1} demonstrated the cyano group of melamine. Moreover, the peaks displayed at 1022 and 817 cm^{-1} in both MOFs were attributed to the triazine ring of melamine.[27] The peak revealed at 755 cm^{-1} in MTGd MOF indicated the bending O–H group, which was shifted to 785 cm^{-1} in the modified MOF. This is due to the hydrogen bond between the hydroxyl group of oxalic acid and melamine during modification.[29,30,33] Lastly, peaks at 518 and 435 cm^{-1} in both MOFs are characteristic peaks for metal bond (Gd–O), demonstrating the presence of Gd–O linkage in both MOFs.[34]

UV analysis

The UV spectra of MTGd and MTGd–OX MOFs samples are represented in (Fig. S2a). The plots demonstrated that both MOFs exhibited absorption bands in the UV range, and no absorption bands were observed in the visible region. MTGd MOF displayed three distinct bands at 219, 264, and 313 nm, with the maximum absorption (λ_{max}) occurring at 313 nm. Conversely, MTGd–OX MOF exhibited absorption bands at 218, 266, and 311 nm, with a λ_{max} of 311 nm. The shift in λ_{max} from 313 to 311 nm in MTGd–OX MOF can be assigned to ethanedioic acid, which is used for modification. This influenced the level of energy gap that exists between HOMO and LUMO orbitals. The process led to a decrease in the rigidity of MTGd–OX MOF, diminishing molecular conjugation and widening the E_{gap} through HOMO and LUMO orbitals. As a result, the absorption energy of MTGd–OX MOF surpassed that of the original MOF, causing a hypochromic change.[35] Band gap energy values for MTGd and MTGd–OX MOFs are to be 3.68 and 3.70 eV, respectively, as depicted in (Fig. S2b).

^{1}H-NMR spectra. Six signals are revealed at δ 2.51, 4.28, 6.38, 7.19, 8.06, and 11.19 ppm in the ^{1}H NMR spectrum for MTGd MOF (Fig. S3a). Whereas seven signals at δ 2.5, 4.88, 6.75, 7.78, 8.04, 8.07, and 11.19 ppm in the ^{1}H NMR were displayed in the spectrum of MTGd–OX MOF (Fig. S3b). The solvent (DMSO) was identified at 2.5 ppm.[36] Moreover, the broad signals that appeared at 4.28 ppm for unmodified MOF, and at 4.88 ppm for modified ones are due to the incorporation of water molecules

linked to the MOF structure.[37] The signals displayed at 6.38 and 7.19 ppm for unmodified MOF and at 6.75 and 6.78 ppm for modified MOF. These signals confirmed the presence of an amide connection between the C=O group of the terephthalic acid ligand and the amine group of melamine.[38] The terephthalic acid ligand's hydrogens were identified at 8.06 ppm for unmodified MOF, and 8.04 and 8.07 ppm for the modified one.[36] The carboxylic protons of terephthalic acid were identified as a broad signal at 11.19 ppm.[39] These data are in good agreement with FTIR peaks.

^{13}C-NMR spectra. Three signals were detected in the ^{13}C NMR spectrum of MTGd MOF (Fig. S3c) at δ 39.95, 129.91, and 166.15 ppm. The ^{13}C NMR spectrum of MTGd–OX MOF reveals four signals at δ 39.94, 129.93, 135.00, and 167.23 ppm, as shown in (Fig. S3d). The phenyl group of terephthalic acid displayed the signal at 129.91 ppm for unmodified MOF while at 129.87 and 134.94 ppm for modified MOF.[40] The signal that emerged at 39.95 ppm was ascribed to (DMSO).[41] The carboxylic group O=C–OH revealed signals at 166.15 and 167.23 ppm for unmodified and modified MOFs, respectively. These data are in good agreement with ^{1}H-NMR peaks.

Mass spectra. Fig. S4a and b illustrates the mass spectra of the dissolved MTGd and MTGd–OX MOFs. The analysis covered the mass-to-charge ratio (m/z) range of 50 to 1100. The last ion peak corresponding to the MTGd MOF fragment was observed at 1097 m/z with a little intensity. On the other hand, the last observed ion peak of MTGd–OX appeared at 1084 m/z, also with lower intensity. Thus, the molecular weight of MTGd and MTGd–OX MOFs couldn't be confirmed *via* both peaks as the spectrum range is limited from 50 to 1100 m/z. Based on the other analysis tools and the fragmentation approach, the most probable proposed structures show a higher molecular weight of different than that of the last observed lower intensity peaks in the spectrum. The most intense peaks in the spectra were recognized at 148 and 218 m/z for MTGd and MTGd–OX MOFs, respectively. From the proposed mass fragmentations for the monomeric units of MTGd and MTGd–OX MOFs (Fig. S5 and S6), the mass spectral fragmentation patterns of both MOFs were examined, and most of the theoretically predicted fragments are in good agreement with the observed m/z values. The observed differences in the base peak ion's masses between the MTGd and MTGd–OX MOFs indicate different molecular structures. This difference, combined with other analysis data, indicates the success of the oxalic acid-induced modification.

XPS analysis. Fig. 4 and 5 represent the X-ray photoelectron spectroscopy for MTGd, MTGd–OX, and MTGd–OX–Eu MOFs. The XPS survey of MTGd MOF (Fig. 4) reveals the presence of Gd, C, N, C 1s, and O. The binding energies of Gd 4d, C 1s, N 1s, O 1s, O(KLL), and Gd 3d were observed at 144.12, 285.72, 402, 533, 975, and (1188.52, 1222.66) eV, respectively. After modifying the MTGd MOF using oxalic acid, the C and O percentages increased due to oxalic acid being linked to the MTGd MOF during the modification process. The XPS survey of the modified MTGd MOF (Fig. 4) shows the presence of Gd, C, N, and O. The binding energies of Gd 4d, C 1s, N 1s, O 1s, O(KLL), and Gd 3d were observed at 144.68, 284.32, 397.66, 533.11, 976.11, and (1188.52, 1220.98) eV, respectively. The XPS survey of the
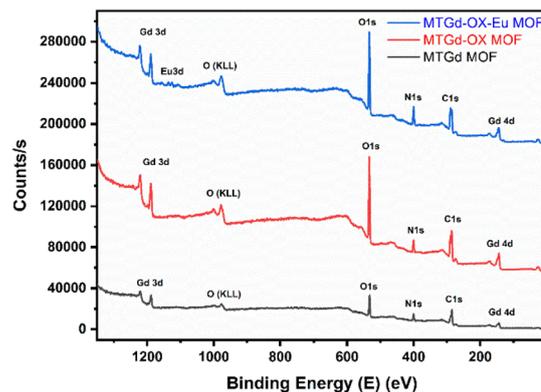

Fig. 4 XPS survey analysis of MTGd, MTGd–OX, and MTGd–OX–Eu MOFs.

MTGd–OX–Eu MOF (Fig. 4) shows the presence of Gd, C, N, O, and Eu. The binding energies of Gd 4d, C 1s, N 1s, O 1s, O(KLL), Eu 3d, and Gd 3d were observed at 144.12, 288.80, 401.02, 533.11, 976.67, (1124.72, 1135.35), and (1188.52, 1219.58) eV, respectively. Eu's presence in the MTGd–OX MOF structure indicates its capability to retain [152+154]Eu from active waste. The increase in C and O percentages after modification with oxalic acid reflected that the efficiency of the MTGd–OX MOF in removing Eu ions from water can be enhanced.

The high-resolution XPS spectra for C 1s, O 1s, and N 1s of MTGd, MTGd–OX, and MTGd–OX–Eu MOFs are represented in (Fig. 5). It provides important details about the chemical composition of the MTGd, MTGd–OX, and MTGd–OX–Eu MOFs (Fig. 5). The MTGd MOF's C 1s XPS spectrum (Fig. 5a) reveals three signals at binding energies of 284.30, 284.6, and 288.49 eV, which were associated with the presence of the carboxylic (O=C–O), aromatic (C=C), and C–C groups, respectively. The relative percentages of these function categories are 27.33, 41.59, and 31.08%, respectively. The binding energy of 284.60 eV assigned to C–C signals is compatible with aromatic rings containing sp[2]-hybridized carbon atoms. In the MTGd–OX MOF, the C 1s XPS spectrum (Fig. 5b) shows three signals at binding energies of 284.60, 286.44, and 288.87 eV, which confirms the presence of C–C, C–O, and C=N functional groups, respectively. The relative percentages of these functional groups were found to be 55.52, 2.09, and 42.39%, respectively. The increase in the percentage of C–C functional groups compared to the MTGd MOF is likely due to the presence of oxalic acid during the modification step.

In the MTGd–OX–Eu MOF, the C 1s XPS spectrum (Fig. 5c) shows three signals at binding energies of 288.66, 286.03, and 284.43 eV, corresponding to the presence of C=O, C–O, and C=C, respectively. The relative percentages of these functional groups were found to be 54.38, 4.39, and 40.69%, respectively. The binding energy of the C=O signal was observed at 288.66 eV, which is consistent with the presence of carbonyl groups. The high-resolution XPS spectra for O 1s in the MTGd, MTGd–OX, and MTGd–OX–Eu MOFs (Fig. 5d–f) provide important information about the coordination and bonding of oxygen-containing functional groups. In the MTGd MOF, the O
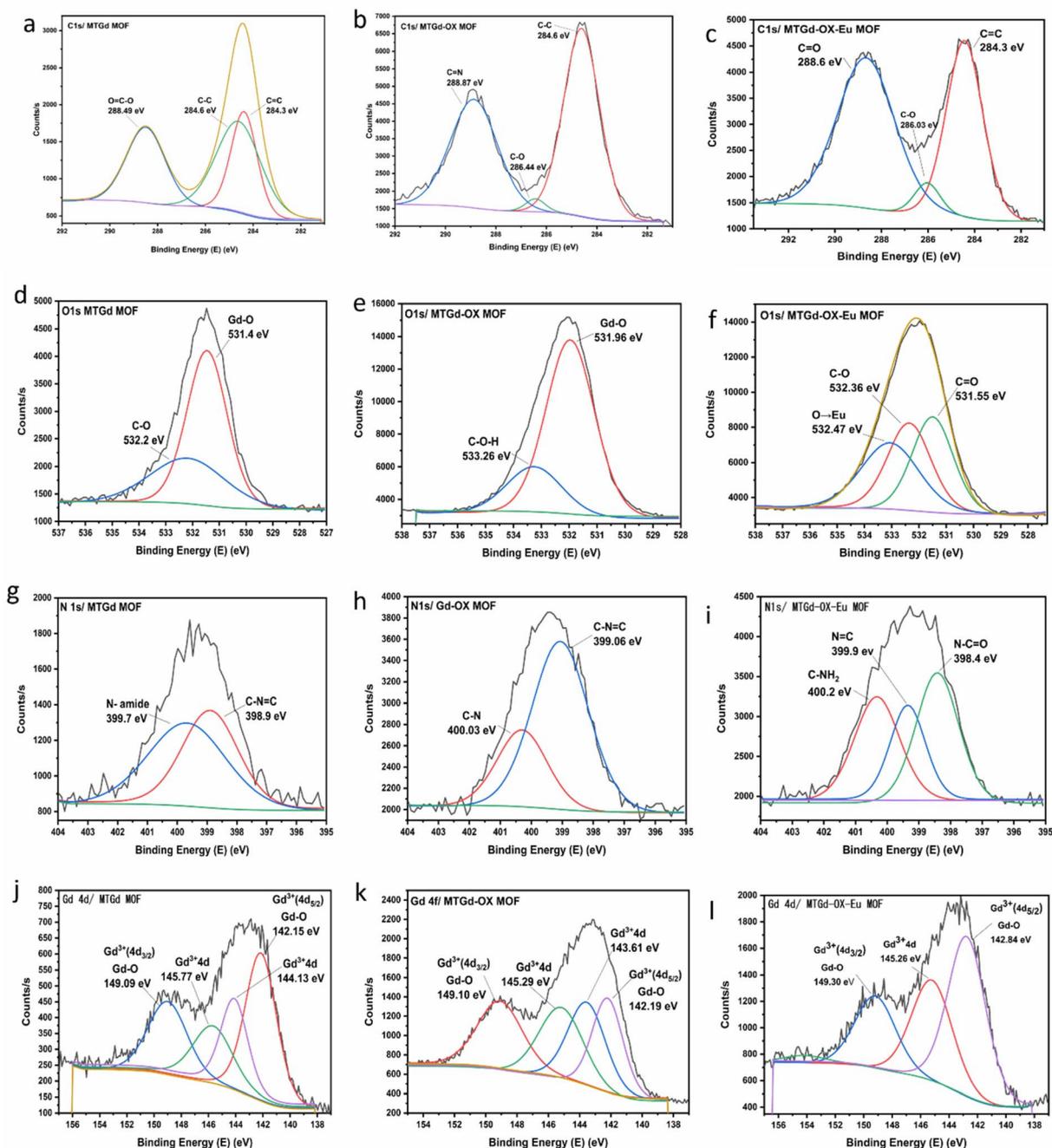
Fig. 5 High-resolution XPS spectra of (a) C 1s–MTGd MOF, (b) C 1s–MTGd–OX MOF, (c) C 1s–MTGd–OX–Eu MOF, (d) O 1s–MTGd MOF, (e) O 1s–MTGd–OX MOF, (f) O 1s–MTGd–OX–Eu MOF, (g) N 1s–MTGd MOF, (h) N 1s–MTGd–OX MOF, (i) N 1s–MTGd–OX–Eu MOF, (j) Gd 4d–MTGd MOF, (k) Gd 4d–MTGd–OX MOF, and (l) Gd 4d–MTGd–OX–Eu MOF.

1s XPS spectrum (Fig. 5d) shows two signals at binding energies of 531.46 and 532.20 eV, which demonstrate the existence of Gd–O (63.44%) and C–O (36.56%), respectively. The Gd–O signal indicates the presence of oxygen coordinated with the gadolinium. While the C–O signal is evidence of the coordination bond between the oxygen from terephthalic acid and gadolinium.

In the MTGd–OX MOF, the O 1s XPS spectrum (Fig. 5e) shows two signals at binding energies of 531.96 and 533.26 eV,

which reveal the presence of Gd–O (76.43%) and C–O–H (23.57%) functional groups, respectively. The appearance of the C–O–H signal after modification is evidence for oxalic acid. The increase in the Gd–O bond is also due to the bonding between the oxygen of oxalic acid and Gd.

In the MTGd–OX–Eu MOF, the O 1s XPS spectrum (Fig. 5f) shows three signals at binding energies of 531.55, 532.36, and 532.47 eV, which demonstrate the presence of Gd–O (25.48%), C–O (43.28%), and Eu–O (31.24%), respectively. The presence of

the Eu–O signal at 532.47 eV is strong evidence of the contribution of the carboxylic oxygen in the removal of Eu from the waste and highlights the role of oxalic acid in the decontamination of Eu. The high-resolution XPS spectra for N 1s in the MTGd, MTGd–OX, and MTGd–OX–Eu MOFs (Fig. 5g–i) provide important information about the nature of nitrogen. In the MTGd MOF, the N 1s XPS spectrum (Fig. 5g) shows two signals at binding energies of 398.90 and 399.70 eV, for C–N=C (40.49%) and O=C–N– (59.51%), respectively. The presence of O=C–N– indicates the formation of amide linkages between the amine groups of melamine and the carboxylic groups of terephthalic acid. In the MTGd–OX MOF, the N 1s XPS spectrum (Fig. 5h) shows two signals at binding energies of 399.06 and 400.30 eV, which demonstrate the appearance of C–N=C (71.07%) of the triazine ring of melamine and C–N (28.93%), respectively. In the MTGd–OX–Eu MOF, the N 1s XPS spectrum (Fig. 5i) shows three signals at binding energies of 398.42, 399.90, and 400.20 eV, which reveal the presence of O=C–N– (43.21%), N=C (19.76%), and C–N (37.03%), respectively. The O=C–N– signal indicates the presence of carboxamide groups, and the N=C signal suggests the presence of an imine linkage in the triazine ring of the melamine ligand.

Gd 4d in MTGd, MTGd–OX, and MTGd–OX–Eu MOFs provides valuable information about the oxidation state and coordination environment of Gd ions in these MOFs. Whereas, the signals at 142.15, 142.19, and 142.84 eV proved the presence of Gd $4d_{5/2}$ (Gd–O). The signals at 142.15 and 149.09 eV in MTGd MOF correspond to Gd^{3+} $4d_{5/2}$ (Gd–O) and Gd^{3+} $4d_{3/2}$ (Gd–O), respectively (Fig. 5j).[42] Similarly, in MTGd–OX MOF, the signals at 142.19 and 149.10 eV correspond to Gd^{3+} $4d_{5/2}$ (Gd–O) and Gd^{3+} $4d_{3/2}$ (Gd–O), respectively (Fig. 5k). The fact that there is no signal at 149.09 eV in MTGd–OX–Eu MOF signifies that the coordination environment of Gd is slightly different from that in MTGd–OX MOF.

The high-resolution XPS spectrum of MTGd–OX–Eu MOF provides valuable information about the oxidation states and coordination environment of Eu^{3+} ions (Fig. 6a). The signals at 1132 and 1136 eV represent the presence of Eu^{3+}, whereas the signals at 1126, 1149, and 1154 eV represent the presence of Eu^{2+}.[43,44] During the adsorption of Eu^{3+} onto MTGd–OX MOF, the O and N atoms can donate electrons to Eu^{3+}, causing a reduction of Eu^{3+} to Eu^{2+}. The presence of Eu^{2+} can be attributed to a ligand-to-metal charge transfer (LMCT) process between the O and N atoms of the bi-ligands and the Eu.[45] The presence of Eu^{3+} and Eu^{2+} indicates that a redox reaction has been carried out.

XRD analysis. Fig. 6b presents the X-ray diffraction patterns of the synthesized Gd-MOF, Gd-OX-MOF, and Gd–OX–Eu-MOF. The XRD peaks of MTGd-MOF closely match the COD database code (4113531).[46] The XRD pattern of the synthesized MTGd MOF was correlated with structurally similar entries in the Crystallography Open Database (COD) due to the novelty of the material and the absence of a common reference pattern (e.g., ICDD or COD) for direct comparison. The XPert-High score program was implemented, and this approach facilitated the derivation of approximations from crystallographic data by identifying similar structural analogies, thereby offering insight
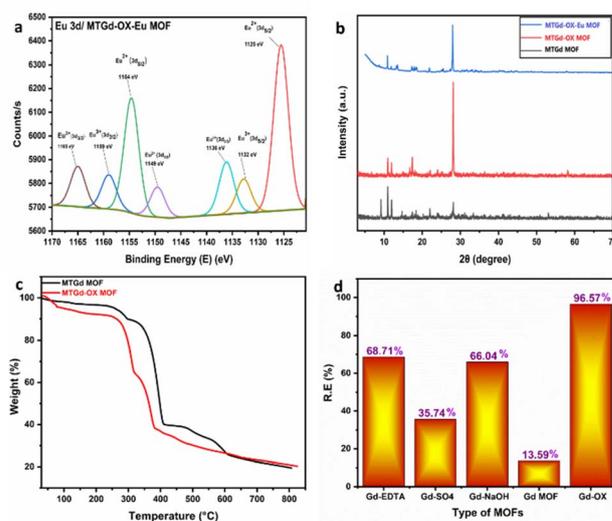

Fig. 6 High-resolution XPS spectra of Eu 3d of MTGd–OX–Eu MOF (a), XRD patterns of MTGd, MTGd–OX, and MTGd–OX–Eu MOFs (b), TGA spectra of MTGd and MTGd–OX MOFs as a function of temperature at a heating rate of 10 °C min⁻¹ in an N_2 ambient (c), and comparison between the removal efficiency of MTGd MOFs (d).

into the potential crystal structure and lattice properties of the synthesized MOFs. Moreover, the XRD pattern of Gd–OX-MOF displays a little bit of shift in peak positions, and intensity changes in the XRD patterns suggest structural adjustments where the core crystal framework remains preserved, with the most prominent peak at $2\theta = 10°$ constantly appearing in all samples. The functionalization process did not result in amorphization, maintaining the MOF's integrity, and confirming the successful incorporation of oxalic acid.[28,33,47,48] The XRD spectrum of Gd–OX–Eu MOF shows a similar spectrum to Gd–OX-MOF with a new peak at $2\theta = 13.5°$, proving the presence of Eu in the MOF structure.[49] Although the lower intensity of the peak at $2\theta = 17.25°$ in MTGd–OX–Eu MOF is observed, MTGd–OX and MTGd–OX–Eu exhibit similar patterns. This result prove that both MOFs are stable in acidic media, and there is no MOF loss when they adsorb in highly acidic radioactive waste. The three spectra exhibit a prominent peak around $2\theta = 10°$,[50] indicating the presence of Gd in pristine MOF, modified MOF, and modified MOF after Eu removal. Compared to the literature data, Luan et al., reported that there is no change in the XRD pattern of the composite Cr-MIL-101-NH$_2$ PCM after functionalization with stearic acid (SA) and the integration of SA with Cr-MIL-101-NH$_2$ is a simple physical mixing without affecting the crystallinity.[33] Furthermore, Hu et al., reported that the XRD pattern of the sulfonic acid(s)-functionalized MIL-101 is similar to the XRD pattern of NH$_2$-MIL-101(Al), indicating that the functionalization method maintains the crystalline structure. These data are consistent with the finding that there were no appreciable changes in XRD pattern crystallinity during the preparation.[47]

Thermal stability analysis. The thermal stabilities of MTGd and MTGd–OX MOFs were examined at a rate of 10 °C min⁻¹ under nitrogen gas up to 800 °C (Fig. 6c). The thermal

investigation shows that the decomposition of both MOFs is carried out in four stages. In the first stage, when the temperature reached 150 °C, a weight loss of about 2.5 and 6.5% was obtained for MTGd and MTGd–OX MOFs, respectively. This is attributed to the water and solvent contents. In the second stage, when the temperature increased to around 300 °C, the weight loss of about 6.5 and 29% for MTGd and MTGd–OX was obtained, respectively. This can be attributed to phase change or water crystallization. In the third stage, upon temperature reaching about 400 °C, a loss of weight is 51 and 24% for MTGd and MTGd–OX occurred, respectively. This can be attributed to the loss of phenyl molecules of MOF during decomposition. At the temperature of 400–600 °C, a loss of weight of about 12 and 13% for MTGd and MTGd–OX was obtained, respectively, which was attributed to the decomposition of the bridging ligand MOF. At 600 °C, the loss of weight is 28 and 27% for MTGd and MTGd–OX, respectively. The remaining residual is about 20 and 21% for MTGd and MTGd–OX, representing the Gd metal content, respectively. These results in a satisfactory agreement with the previous data.[51] Because Gd^{3+} is harder, high charge density and a relatively smaller ionic radius than Sr^{2+}, according to HSAB theory. Therefore, it is likely to be better able to form strong and stable coordination bonds with solid donor atoms such as carboxylates. This can improve the thermal stability of Gd-based MOFs. The results of the thermogravimetric analysis (TGA) corroborate this finding by demonstrating that Gd-MOFs have a much greater residual mass compared to MTSr-MOFs.[16,52] This indicates that their structure is more robust and resistant to heat.

BET analysis. The MTGd and MTGd–OX N_2 adsorption–desorption isotherms are displayed in (Fig. S7a). As noticed, both MOFs had a type IV isotherm with a hysteresis loop at 0.44–0.85P/P_0, suggesting the presence of a micro–mesoporous structure (1.60–6.72 nm). The samples under examination exhibited an increase in adsorption isotherms throughout the relative pressure range of 0.4–0.9P/P_0, suggesting the presence of mono-molecular layer adsorption on the MOF surface. Subsequently, the adsorption curves witnessed a sharp increase, leading to the saturation of adsorption in the mono-molecule layer and afterward in the multi-molecule layer. This matches the data from the Freundlich model to describe the sorption process that occurs via multilayer adsorption onto a heterogeneous surface with varying adsorption energy.[52–54] According to the analysis, MTGd and MTGd–OX MOFs have BET surface areas of 1857.40 and 1955.16 m^2 g^{-1}, respectively, demonstrating the remarkable surface area of the synthesized MOFs. The modified MOF's BET surface area is more than it was before the modification.[55] This illustrates how the modification affects the MOF's ability to adsorb molecules by expanding its surface area. However, the pore size of the two MOFs is 1.6 nm, which demonstrates the remarkable porosity of the synthesized MOFs. The similarity in the pore size distribution of the two MOFs indicates that the modification with oxalic acid does not affect the pore size and is just surface modification. Additionally, the surface area was calculated using various methods, and the results are tabulated in (Table S1). Using the BJH, DH, DR,

DFT, HK, and SF techniques, the pore size distribution (Fig. S7b) of both MOFs was calculated (Table S2).

Based on the correlation between the characterization tools results, the TGA was used to calculate the metal ion percent in the prepared MOFs, as well as the functional groups that were recognized as a result of the FT-IR and XPS data. Moreover, the ^{13}C and ^{1}H NMR's results were utilized to identify the type of carbon bonding and MOF protons, and the proposed structure was optimized following the mass spectroscopy fragmentation's results. In addition, the elemental analysis results given from CHN, EDX, and XPS were used to aid in describing the MOF structure. The proposed structural model suggests surface modification via hydrogen bonding between oxalic acid and the amine groups of the melamine ligand within the MOF. The proposed 3D structures of the monomeric unit for both MTGd and MTGd–OX MOFs were represented in (Fig. S8 and S9), respectively.

Sorption studies

Preliminary experiments. The synthesized MTGd MOF was used to remove radioactive [152+154]Eu and demonstrated a good removal of approximately 68.71%. The MTGd MOF was treated with a variety of modifiers, including EDTA, H_2SO_4, NaOH, and oxalic acid. The MTGd MOF and other modified MOFs were used to remove the radioactive [152+154]Eu. Among all of them, oxalic acid-modified MOF exhibited the highest removal ability (96.57%) (Fig. 6d). Thus, all our studies on the elimination of [152+154]Eu utilized MTGd–OX MOF and will be explored in detail.

Effect of pH. To evaluate how pH affects the sorption of [152+154]Eu radionuclides with MTGd–OX MOFs, (Fig. 7a) shows a relationship between pH value and radionuclides removal efficiency. The results show that increased pH levels improved the separation of Eu ions. At lower pH levels, protons actively compete with available sites on the MTGd–OX MOF surface, hindering the adsorption of [152+154]Eu radionuclides. Conversely, with an increase in pH, the competition diminishes, leading to an enhanced removal efficiency of [152+154]Eu radionuclides using the MTGd–OX MOF. Consequently, all investigations were conducted at a pH of 3.5. The final pH values significantly dropped during [152+154]Eu separation by the MTGd–OX MOF.[16] This decrease in pH value suggests that the release of protons from the MTGd–OX surface sites and that the [152+154]Eu ions are being separated by an ion exchange process.

Contact time effect. The investigation into the uptake of Eu ions by MTGd–OX MOF utilized a batch-based technique (Fig. 7b). The removal efficiency witnessed a dramatic increase through the first hour, followed by a little increase until the peak at 97%, then equilibrium was achieved. The rapid initial sorption is ascribed to the prompt binding of active sites on the MTGd–OX MOF with [152+154]Eu ions, facilitating swift uptake. As the sorption advanced and surface coverage increased, the available sorption sites on the MOF diminished. This intensified the competition among ions for the remaining sites and decelerated the sorption process. Through the initial 120 minutes of contact time, the majority of ions were absorbed, leading to a 94% removal efficiency after 4 hours, and
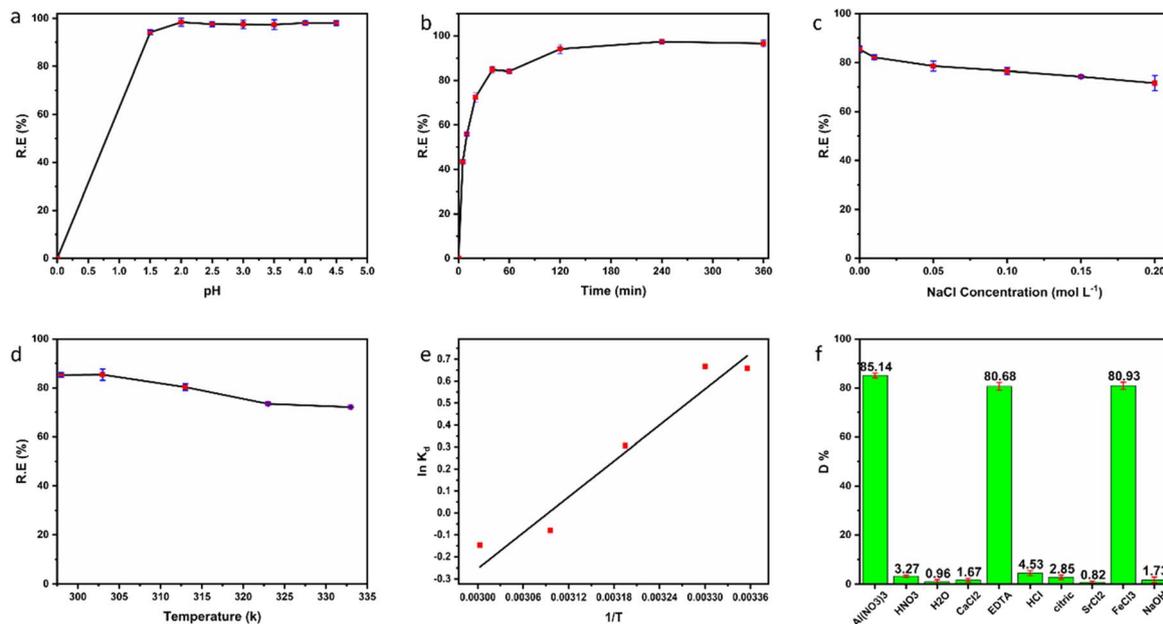
Fig. 7 Effect of pH on the sorption process of $^{152+154}$Eu (t_e = 4 h; C_i = 20 mg L^{-1}; m/V = 6 g L^{-1}; temp. = 25 °C) (a), the effect of contact time on the sorption process of $^{152+154}$Eu (C_i = 20 mg L^{-1}, pH$_i$ = 3.5, m/V= 6 g L^{-1}, temp. = 25 °C) (b), the effect of ionic strength on the sorption process of $^{152+154}$Eu (t_e = 4 h; C_i = 80 mg L^{-1}; pH$_i$ = 3.5; m/V= 3 g L^{-1}; temp. = 25 °C) (c), the effect of temperature on the sorption process of $^{152+154}$Eu (t_e = 4 h; C_i = 80 mg L^{-1}; pH$_i$ = 3.5; m/V= 3 g L^{-1}) (d), the thermodynamic study of $^{152+154}$Eu sorption onto MTGd–OX MOF (e), and the desorption of the prepared MTGd–OX MOF after $^{152+154}$Eu sorption (t_e = 4 h; C_i = 20 mg L^{-1}; pH$_i$ = 3.5; m/V = 6 g L^{-1}; temp. = 25 °C) (f).

approximately remaining unchanged with elapsing time. Therefore, it was decided that a contact time of four hours would be the ideal duration for the trials that proceeded.

Ionic strength effect. Fig. 7c illustrates the results revealed during the study of the impact of the ionic capacity of the aqueous solution on the separation of Eu ions, with NaCl acting as an ambient electrolyte with a concentration ranging from 0.01 to 0.2 mol L^{-1}. The removal percentage of Eu(III) onto the MOF was slightly affected by the presence of NaCl, leading to a reduction in the MOF's affinity for Eu(III). This minimal influence of NaCl on the sorption of Eu(III) suggests a slight hindrance in the migration of Eu(III) from the bulk solution to the surface of the sorbent.[56]

Temperature effect. To explore the temperature influence on $^{152+154}$Eu radionuclides separation utilizing MTGd–OX MOF, a series of experiments was conducted from 298–333 K. The results shown in (Fig. 7d) revealed a negative impact of temperature on the separation of europium. As the temperature increased, the separation of $^{152+154}$Eu using MTGd–OX MOF decreased. These results point to an exothermic removal process. The decrease in the removal efficiency at higher temperatures suggests that the sorption of $^{152+154}$Eu onto MTGd–OX MOF was less advantageous under elevated temperature conditions, indicative of an escalated energy requirement for the sorption process.

MTGd–OX maximum sorption capacity. The batch technique was employed to study the maximum sorption capacity of MTGd–OX MOF. A 5 mL solution containing stable europium with a 200 mg L^{-1} concentration spiked with traces of radioactive $^{152+154}$Eu was mixed with 0.03 g of MTGd–OX MOF. The

mixture was shaken until equilibrium was reached at 25 °C. After reaching equilibrium, the sorption capacity (q_e) of MTGd–OX MOF was calculated using eqn (3). The maximum sorption capacity of MTGd–OX MOF for $^{152+154}$Eu (eqn (1)):

$$Q_{max} = \sum_{e=1}^{n} q_e \tag{1}$$

where e, or 1, 2, 3…n, is the number of asserted equilibrations. The level of maximum sorption capacity of the prepared MOF was determined and found to be 37.22 mg g^{-1}.

Sorption kinetic models

Several kinetic models, including pseudo-first-order (Fig. S10), pseudo-second-order models (Fig. S11), and particle-diffusion (Fig. S12) were used to explore the kinetics of Eu sorption onto the MTGd–OX MOF surface. The summary of kinetic parameters for sorption of $^{152+154}$Eu onto MTGd–OX MOF were presented in Table 1 (more information about the sorption kinetic models (Appendix A) in the SI file).

Sorption isotherm models

The main goal of the study of sorption isotherm models is to determine the correlation between the concentration of metal ions and the equilibrium amount of adsorbed ions on a solid surface. Various parameters connected with sorption isotherms were investigated to determine the surface properties and affinity of the prepared MOF. Several isothermal models (Fig. S13–S16) were utilized to examine the $^{152+154}$Eu removal over a dosage from 10 to 200 mg L^{-1}. The summary of the

Table 1 Kinetic parameters for sorption of $^{152+154}$Eu onto MTGd–OX MOF

Kinetics models	Parameters	Values
Pseudo-first-order	$K_1 \times 10^{-2}$, min^{-1}	2.27
	q_e, calc., mg g^{-1}	1.55
	q_e, exp., mg g^{-1}	2.26
	R^2	0.9436
Pseudo-second-order	$k_2 \times 10^{-2}$, g mg^{-1} min^{-1}	6.87
	q_e, calc., mg g^{-1}	3.25
	q_e, exp., mg g^{-1}	2.26
	R^2	0.9999
Intra-particle diffusion	k_{dif}, mg g^{-1} min^{-1}	0.54
	C, mg g^{-1}	3.18
	R^2	0.9871

Table 2 Parameters of the Freundlich, Langmuir, Temkin, and Dubinin–Radushkevich for sorption of $^{152+154}$Eu onto MTGd–OX MOF

Isotherm model	Parameters	Values
Freundlich	K_F	4.96
	n	1.89
	R^2	0.9974
Langmuir	Q_m (mg g^{-1})	35.21
	$b \times 10^{-2}$ (L mg^{-1})	12.66
	$R_L \times 10^{-2}$	28.30
	R^2	0.9454
Temkin	A (L g^{-1})	2.44
	b_t (kJ mol^{-1})	0.42
	B	5.89
	R^2	0.9043
Dubinin–Radushkevich	Q_{max} (mg g^{-1})	14.69
	$\beta \times 10^{-6}$ (mol^2 kJ^{-2})	0.02
	E (kJ mol^{-1})	5.00
	R^2	0.7794

parameters of the Freundlich, Langmuir, Temkin, and Dubinin–Radushkevich for sorption of $^{152+154}$Eu onto MTGd–OX MOF were presented in Table 2 (more information about the sorption isotherm models (Appendix B) in the SI file).

Thermodynamic studies

The thermodynamic assessment of the sorption process for $^{152+154}$Eu encompassed the computation of Gibbs free energy ($\Delta G°$), enthalpy change ($\Delta H°$), and entropy change ($\Delta S°$). Fig. 7e illustrates the intercept and slope derived from the linear plot of ln K_d against $1/T$. These thermodynamic parameters were determined using eqn (2).[57]

$$\ln K_d = \frac{\Delta S°}{R} - \frac{\Delta H°}{RT} \tag{2}$$

Gibbs free energy ($\Delta G°$) could be calculated using the following eqn (3):

$$\Delta G° = \Delta H° - T\Delta S° \tag{3}$$

Table 3 shows a negative $\Delta H°$ value, which indicates that the separation of Eu ions on MOF is exothermic. The negative $\Delta G°$

Table 3 Thermodynamic parameters for sorption of $^{152+154}$Eu onto MTGd–OX MOF

Temperature (K)	$\Delta G°$ (kJ mol^{-1})	$\Delta H°$ (kJ mol^{-1})	$\Delta S°$ (kJ mol^{-1} K^{-1})
298	−1.78	−21.85	−0.067
303	−1.44		
313	−0.76		
323	−0.09		
333	0.58		

values support the thermodynamic feasibility and spontaneity of the sorption process for $^{152+154}$Eu. Furthermore, during the sorption process, a decreasing random nature is suggested by the negative $\Delta S°$ value. These results are consistent with a lower temperature rise in sorption.[58]

Desorption studies

Fig. 7f shows the desorption behaviour of $^{152+154}$Eu from loaded MTGd–OX MOF with different eluents to improve MOF's efficiency for the separation of radioactive ions. The data show that $^{152+154}$Eu was hardly eluted from MTGd–OX MOF using pure water, NaOH, CaCl$_2$, SrCl$_2$, HCl, HNO$_3$, and citric acid. Using 0.1 mol per L Al(NO$_3$)$_3$, a large desorbed amount of $^{152+154}$Eu from MTGd–OX MOF was observed. This behaviour could be related to the cationic exchange of Al^{3+} and Eu^{3+} ions. It is often assumed that hydrated Al^{3+} ions have a smaller ionic radius than Eu^{3+}. As a result of its high electronegativity and low ionic radius, Al^{3+} ions could easily diffuse into the MOF's inner structure, effectively replacing Eu^{3+} ions and eventually eluting it from loaded MTGd–OX MOF.[59]

Sorption mechanism of $^{152+154}$Eu onto MTGd–OX MOF

In the MTGd–OX–Eu MOF, the O 1s XPS spectrum (Fig. 5f) shows the signal at a binding energy of 532.47 eV, which demonstrates the presence of Eu–O. The presence of the Eu–O signal is strong evidence of the contribution of the carboxylic oxygens in the removal of Eu from the waste and highlights the role of carboxylic groups of oxalic acid in the decontamination of Eu ions. In MTGd–OX–Eu MOF (Fig. 6a), the presence of Eu^{2+} is indicated by the signals at 1126, 1149, and 1154 eV.[43,44] The presence of Eu^{2+} indicates that a redox reaction has been induced on Eu ions due to the coordination environment provided by the bi-ligands in MTGd–OX MOF. The presence of Eu^{2+} can be attributed to a ligand-to-metal charge transfer (LMCT) process between the O and N atoms of the bi-ligands and the Eu ions.[45]

It should be noted that the final pH values fell along with the sorption of $^{152+154}$Eu onto MTGd–OX MOF. This decrease in pH values shows that hydrogen protons were released from the MTGd–OX MOF surface sites in the aqueous solution as a result of the uptake of $^{152+154}$Eu ions. There is a possibility that an ion exchange mechanism could be responsible for the removal of $^{152+154}$Eu. Moreover, using Al(NO$_3$)$_3$, a significant desorbed amount of $^{152+154}$Eu from MTGd–OX–Eu MOF was observed. This behaviour could be related to the cationic exchange of Al^{3+}

Table 4 Sorption capacities comparison of MTGd–OX MOF with other different materials

Adsorbents	pH	Capacity (mg g^{-1})	Reference
MTGd MOF	3.5	2.27	This work
MTGd–OX MOF	3.5	37.22	This work
MTSr–OX MOF	3.5	234.72	16
MTSr MOF	3.5	54.36	26
UiO-66-PO$_4$		58	61
Al^{3+}- and Fe^{3+}-doped zirconium and titanium phosphates	3.0	20–30	62
Gaomiaozi bentonite	4.1	42.1	63
Cellulose-based silica	6.0	24	64

and Eu^{3+} ions. Therefore, there is a possibility that the ion exchange mechanism could be responsible for the removal of $^{152+154}$Eu sorption using the Dubinin–Radushkevich model since the estimated value of E for $^{152+154}$Eu is 5 kJ mol^{-1}. This calculated energy value is comparable to the physical sorption that indicates reversible adsorption and typically occurs at low temperatures, demonstrating the ion exchange behaviour of MOF.[60]

Therefore, the removal mechanism of Eu by MTGd–OX MOF is believed to be a combination of a charge transfer bonding between the MOF ligands and Eu ions as well as an ion exchange with MOF protons.

Real application

Table 4 shows a higher removal capacity of MTGd–OX MOF for Eu than many other reported adsorbents in highly acidic conditions (pH = 3.5).[16,26,61–64]

On the other hand, (Fig. 8) shows the potential of MTGd–OX MOF to remove cesium (^{134}Cs; 92.66 keV), europium ($^{154+152}$Eu; 312.17, and 718.77 keV), iodine (^{131}I; 633.32 keV), molybdenum (^{99}Mo; 176.30 keV), strontium (^{89}Sr; 500.80 keV), and technetium (^{99}Tc; 139.88 keV) from the real sample. The removal efficiencies were as follows: 53.5% for ^{134}Cs, 56.3% for ^{152}Eu, 49.1% for ^{99}Tc, 100% for ^{154}Eu, 100% for ^{99}Mo, 56% for ^{131}I, and 54.4% for ^{89}Sr. These results indicate that MTGd–OX MOF had promising performance in removing isotopes of technetium,

molybdenum, strontium, europium, iodine, and cesium from a radioactive real waste sample. The MTGd MOFs revealed a lower adsorption behaviour when compared to MTSr MOFs; this can be attributed to Gd-MOFs having a tighter network structure, a higher coordination number, and electrostatic attraction. Which makes them denser than MTSr MOFs. As a result, a higher mass-to-volume ratio of MTGd–OX was required to improve adsorption; a ratio ten times higher than that of MTSr–OX was utilized. Subsequently, the removal efficiency (R.E.) was affected. Furthermore, the average pore diameter of MTSr–OX (1.7 nm) is slightly larger than that of MTGd–OX (1.6 nm), supporting higher Eu^{3+} diffusion and greater availability within the Sr-based MOF framework. Finally, good removal efficiency was observed for several isotopes.

Experimental

Chemicals and reagents

All chemicals and reagents were used without purification. The radioactive $^{152+154}$Eu material was created by being exposed to neutrons at the ET-RR-2 Egyptian nuclear power plants.

Instruments and sample preparation for analysis

The MTGd and MTGd–OX MOFs were characterized by various methods. Carbon, hydrogen, and nitrogen elements were measured using a Costech ECS-4010 analyzer with a detection range of 200 ppm and a sample volume of 10 mg in a metal canister. Fourier transform infrared (FT-IR) spectroscopy was performed on a JASCO 3600 using the potassium bromide (KBr) granule method in the 400–4000 cm^3 range. This method involves finely grinding a MOF sample of approximately 1–2 mg with high-quality KBr and then compressing it into a transparent disc. For ^{1}H and 13-nuclear magnetic resonance (NMR) spectroscopy, the sample was mixed with deuterium dimethyl sulfoxide (DMSO-d$_6$), and the spectra were recorded using a 300 MHz Gemini spectrometer (ECA 500 II, JEOL, Japan). Approximately 10 mg of MOF was mixed with 0.6 mL of DMSO-d$_6$ and subjected to ultrasonication for 15 minutes to ensure even mixing or dissolution. The spectrum showed solvent bands similar to DMSO. For calculating the mass, a Thermo Scientific ISQ quadrupole was used. MOF samples were mixed with methanol or DMSO and then put right into the ion source to make positive ions at the electrode. A TA Instruments SDT Q600
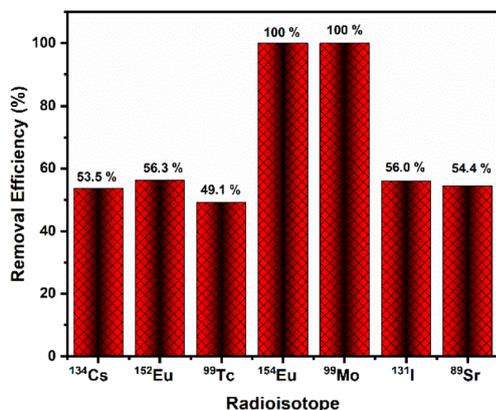

Fig. 8 Removal behavior of the MTGd–OX MOF toward Cs, Eu, I, Sr, Tc, and Mo.

was used for thermogravimetric analysis (TGA) to check the temperatures. 5–10 mg of the samples was heated from room temperature to 800 °C at a rate of 10 °C min^{-1} in a nitrogen atmosphere. UV/visible absorption bands were measured using a JASCO V-570 spectrometer. Samples were dissolved or dispersed in ethanol and then analyzed in a 1 cm path length quartz cuvette. The diffuse reflectance pattern of the solid was also used when dissolution was not possible. The chemical state and elemental presence were analyzed by X-ray photoelectron spectroscopy (XPS) using a Thermo Scientific K-Alpha. The solid samples were mounted on carbon tape electrodes and analyzed in an ultrahigh vacuum without any chemical change. Mass analysis was performed using a Thermo Scientific ISQ quadrupole. MOF samples were mixed with methanol or DMSO and directly introduced into the ion source to generate positive electrode ions. Thermal stability was tested using thermogravimetric analysis (TGA) on a TA Instruments SDT Q600. 5–10 mg of samples were heated from room temperature to 800 °C at a rate of 10 °C min^{-1} under nitrogen. Powder X-ray diffraction (XRD) patterns were obtained using a Bruker AXS D8 X-ray diffractometer (Germany) using Cu-Kα radiation ($\lambda = 1.5406$ Å). The scanning speed was 0.4 s per step, and the step size was 0.02° over a range of 3–70°. Samples were smoothed on a background-free holder to ensure uniform surface reflection throughout. A JEOL JSM-6510LV microscope (Japan) was used for scanning electron microscopy (SEM) images. Solid MOF powders were mounted on carbon tape without any additional processing or coating. High-resolution transmission electron microscopy (HR-TEM) images were captured using a JEM-2100 camera (JEOL, Japan). Samples were ultrasonicated, mixed with ethanol, drop-cast onto carbon-coated copper plates, and air-dried. No staining or other treatment was performed. BET surface area and pore size distribution were measured using a Quantachrome at 77.35 K. Samples were degassed at 200 °C for 4 h to remove dimethyl formaldehyde (DMF) molecules and water solvent before analysis. The data was analyzed using the Quantachrome TouchWin version 1.2 software. The radioactivity was quantified using both single-channel and multi-channel gamma monitors. Water-based products that contained radioactive materials were employed as measuring instruments. A Nucleus Model 500 NaI(Tl) scintillation counter and a Model 2010 standard amplifier were employed to accurately detect and locate gamma channels. Calibration and noise adjustment were implemented prior to data acquisition.

Procedures

Synthesis and modification

MTGd MOF synthesis. The hydrothermal synthesis method was employed to create a gadolinium metal–organic framework (MTGd MOF). The synthesis utilized melamine (M), terephthalic acid (T), and gadolinium chloride hexahydrate in a 1 : 1 : 1 molar ratio. The reaction takes place in a mixture of distilled water and DMF (2 : 1 v/v). To initiate the synthesis, 0.158 g (1.0 mmol) of melamine was fully dissolved in 10.0 mL of distilled water, followed by 5.0 mL of DMF. Separately, 0.371 g (1.0 mmol) of GdCl$_3 \cdot$6H$_2$O dissolved in just a few millilitres of water,

and added to the melamine solution, shaking for thirty minutes, resulting in solution-A. Subsequently, 5.0 mL of DMF was used to dissolve 0.166 g (1.0 mmol) of terephthalic acid, which was then added by drops to solution-A while being constantly stirred, causing an immediate appearance of white colour and forming solution-B. To regulate the reaction, 1 mL of glacial acetic acid was added to solution-B, and then shaken for another 30 minutes. Solution-B was transferred to a 200 mL Teflon-lined stainless autoclave and subjected to hydrothermal conditions at 180 °C for 18 hours. After cooling to room temperature, a fine white MTGd MOF powder was obtained, which was subsequently filtered, cleansed with water and DMF to eliminate any lingering impurities, and ultimately subjected to vacuum drying at 60 °C. The final mass of the prepared MOF was 0.30 g, and the theoretical yield was 81.30%.

Functionalization and modification of MTGd MOF. After synthesizing the MTGd MOF using the method described earlier, the resulting material was soaked in solutions containing different modifiers at a concentration of 0.05 mol L^{-1}. These modifiers included EDTA, H$_2$SO$_4$, NaOH, and oxalic acid. The soaking was carried out for 24 hours. The modified MTGd MOFs, namely MTGd–EDTA, MTGd–H$_2$SO$_4$, MTGd–NaOH, and MTGd–OX MOFs, were obtained. These modified samples were subsequently filtered, cleansed with water to eliminate any lingering impurities, and ultimately subjected to vacuum drying at 60 °C.

Sorption investigations. Every inquiry was carried out till its equilibrium had been established, using a batch approach, three duplicates of each experiment were conducted. MTGd MOFs were brought to equilibrium with a $^{152+154}$Eu aqueous solution with different pH values (1–4.5). Various factors, including contact time (5 min up to 6 hours), the optimal mass ratio of MTGd MOF, the temperature range of 25 to 60 °C, and the NaCl ionic strength range of (0.01–0.2 mol L^{-1}) were studied. Thorough mixing was achieved using a thermostatic shaker. Centrifugation was employed to separate the liquid phase from the MOF, and the radiometric measurement of $^{152+154}$Eu activity was conducted. Using eqn (4), the R.E.% of $^{152+154}$Eu was ascertained:

$$\mathrm{R.E.\%} = \frac{A_i - A_f}{A_i} \times 100 \qquad (4)$$

In which prior to and following the sorption process, A_i and A_f stand for the starting and final specific activities for the europium active solution, respectively. To calculate the sorbed amount of $^{152+154}$Eu (q_e, mg g^{-1}) on MOF, apply eqn (5).

$$q_e = \frac{(C_o - C_e) \times V}{m} \qquad (5)$$

The start and final concentrations of $^{152+154}$Eu are shown by the symbols C_o and C_e (mg L^{-1}). The quantity for the MOF in grams is denoted by m, while the volume of the solution in litres is represented by V.

MTGd MOF regeneration. The process of radioisotope desorption was examined using various eluents, 20 mg L^{-1} of $^{152+154}$Eu aqueous solution was mixed with a particular amount

of MOF material for six hours at the proper pH. After separating the supernatants, their radiometric activity was measured. The solid residues were then mixed with 5.0 mL of every one of the 10 solvents: 0.1 mol per L calcium chloride, strontium chloride, ferric chloride, aluminium nitrate, hydrochloric acid, nitric acid, citric acid, ethylene diamine tetra acetic acid, sodium hydroxide, and also distilled water, then shaken for two hours. Subsequently, radiometric assays were conducted on the separated supernatants to assess their activity. Eqn (6) was used to compute the percentage of desorption:

$$D\% = \frac{A_d}{A_i - A_f} \times 100 \qquad (6)$$

In the provided equation, A_i and A_f, represent the initial and final activities of the $^{152+154}$Eu solution before and after sorption, respectively. After the desorption process, A_d, represents the supernatant's activity.

Conclusions

A bi-ligand gadolinium MOF was synthesized and modified using various modifiers and applied for the separation of Eu ions from the active wastes. The prepared materials were characterized using TGA, FT-IR, XPS, ^{13}C and ^{1}H NMR, mass spectroscopy fragmentation, CHN, EDX, and XPS to calculate metal ion percent, optimize functional groups, and describe the MOF structure based on the correlation between characterization tools. On the other hand, based on the BET results, MTGd–OX MOF had a greater surface area than the MTGd MOF, which enhanced the removal behaviour of the modified MOF. In addition, different kinetic models were applied to describe the separation process. The Freundlich model was demonstrated to explain the sorption process. The sorption process was thermodynamically feasible, spontaneous, and exothermic. Moreover, different eluents were employed to elute the loaded $^{152+154}$Eu ions from MTGd MOF, with aluminium nitrate demonstrating the best desorption capacity. MTGd–OX MOF displayed a significant removal towards a range of radionuclides of active waste. At pH 3.5, MTGd–OX MOF outperformed many other reported adsorbents in terms of its capacity to remove Eu. The obtained results indicate that the synthesized MTGd–OX MOF may be suitable as a decontamination material for $^{152+154}$Eu radionuclides waste.

Author contributions

Mohamed A. Hamouda (M. A. H.), Reda R. Sheha (R. R. S.), Said M. El-Sheikh (S. M. E.), A. T. Kandil (A. T. K.), Omnia I. Ali (O. I. A.), and Sheta M. Sheta (S. M. S.): conceptualization, S. M. E., M. A. H., and S. M. S.; methodology, S. M. E., M. A. H. and S. M. S.; validation, M. A. H. and S. M. S.; formal analysis, M. A. H., R. R. S., S. M. E., O. I. A. and S. M. S.; investigation, M. A. H., S. M. E., R. R. S., O. I. A. and S. M. S.; resources, S. M. E., and S. M. S.; data curation, M. A. H., S. M. E. and S. M. S.; writing—original draft preparation, M. A. H., S. M. E. and S. M. S.; writing—review and editing, all authors; visualization, R. R. S., S. M. E., A. T. K., O. I. A., and S. M. S.; project administration, S. M. S.; funding acquisition, S. M. S. All authors have read and agreed to the published version of the manuscript.

Conflicts of interest

There are no conflicts to declare.

Data availability

All data generated or analysed during this study are included in this published article [and its SI files].

The supporting information file contain nine figures, two tables, appendix (A) for sorption kinetic models, appendix (B) for sorption isotherm models, and last section including on sample preparations for the conducted experiments with cited references. See DOI: https://doi.org/10.1039/d5ra02552d.

Acknowledgements

Notes and references

1 K. Patra and A. Sengupta, *Mater. Today Sustain.*, 2024, **25**, 100703.

2 E. A. Gendy, D. T. Oyekunle, J. Ali, J. Ifthikar, A. El-Motaleb Mosad Ramadan and Z. Chen, *J. Environ. Radioact.*, 2021, **238–239**, 106710.

3 R. Novikau and G. Lujaniene, *J. Environ. Manage.*, 2022, **309**, 114685.

4 S. M. Sheta, M. A. Hamouda, O. I. Ali, A. T. Kandil, R. R. Sheha and S. M. El-Sheikh, *RSC Adv.*, 2023, **13**, 25182–25208.

5 R. O. Abdel Rahman, H. A. Ibrahium and Y. T. Hung, *Water*, 2011, **3**, 551–565.

6 J. Li, X. Wang, G. Zhao, C. Chen, Z. Chai, A. Alsaedi, T. Hayat and X. Wang, *Chem. Soc. Rev.*, 2018, **47**, 2322–2356.

7 H. M. Saleh, S. M. El-Sheikh, E. E. Elsayed and A. K. Essa, *Constr. Build. Mater.*, 2019, **223**, 221–232.

8 H. M. Saleh, S. M. El-Sheikh, E. E. Elsayed and A. K. Essa, *Constr. Build. Mater.*, 2019, **200**, 135–145.

9 M. R. Abukhadra, M. H. Eid, M. A. El-Meligy, M. Sharaf and A. T. Soliman, *Int. J. Biol. Macromol.*, 2021, **173**, 435–444.

10 H. Moloukhia, W. S. Hegazy, E. A. Abdel-Galil and S. S. Mahrous, *Chem. Ecol.*, 2016, **32**, 324–345.

11 M. Jiménez-Reyes, P. T. Almazán-Sánchez and M. Solache-Ríos, *J. Environ. Radioact.*, 2021, **233**, 106610.

12 S. M. Sheta, M. A. Hamouda, O. I. Ali, A. T. Kandil, R. R. Sheha and S. M. El-Sheikh, *RSC Adv.*, 2023, **13**, 25182–25208.

13 K. Patra, S. A. Ansari and P. K. Mohapatra, *J. Chromatogr. A*, 2021, **1655**, 462491.

14 S. Ali Akbar Razavi and A. Morsali, *Coord. Chem. Rev.*, 2019, **399**, 213023.

15 Y. Du, X. Jia, L. Zhong, Y. Jiao, Z. Zhang, Z. Wang, Y. Feng, M. Bilal, J. Cui and S. Jia, *Coord. Chem. Rev.*, 2022, **454**, 214327.

16 R. R. Sheha, S. M. Sheta, M. A. Hamouda, S. M. El-Sheikh, A. T. Kandil and O. I. Ali, *J. Environ. Radioact.*, 2023, **270**, 107287.

17 A. S. Basaleh and S. M. Sheta, *J. Inorg. Organomet. Polym. Mater.*, 2021, **31**, 1726–1737.

18 Z.-Q. Bai, L.-Y. Yuan, L. Zhu, Z.-R. Liu, S.-Q. Chu, L.-R. Zheng, J. Zhang, Z.-F. Chai and W.-Q. Shi, *J. Mater. Chem. A*, 2015, **3**, 525–534.

19 Z. Li, Y. Shen, S. Ling and Y. Wang, *Energy Rep.*, 2022, **8**, 335–340.

20 N. Zhang, L. Y. Yuan, W. L. Guo, S. Z. Luo, Z. F. Chai and W. Q. Shi, *ACS Appl. Mater. Interfaces*, 2017, **9**, 25216–25224.

21 R. Raz, H. Levine, O. Pinto, D. M. Broday, Y. Weisskopf and M. G. Weisskopf, *Am. J. Epidemiol.*, 2018, **187**(4), 717–725.

22 S. M. Sheta, S. R. Salem and S. M. El Sheikh, *J. Mater. Res.*, 2022, 1–12.

23 W.-J. Ouyang, M.-Z. Guo, Y. Wang, X.-H. Kong, X.-L. Xiao, C.-M. Nie and G.-W. Peng, *J. Mol. Liq.*, 2024, **397**, 124124.

24 E. D. Miensah, M. M. Khan, J. Y. Chen, X. M. Zhang, P. Wang, Z. X. Zhang, Y. Jiao, Y. Liu and Y. Yang, *Crit. Rev. Environ. Sci. Technol.*, 2020, **50**, 1874–1934.

25 B. Li, M. Bao, Y. Kang, L. Wang, Y. Liu, L. Wang and C. Xu, *Natl. Sci. Open*, 2024, **4**, 20240028.

26 M. A. Hamouda, S. M. Sheta, R. R. Sheha, A. T. Kandil, O. I. Ali and S. M. El-Sheikh, *RSC Adv.*, 2022, **12**, 13103–13110.

27 N. E. Mircescu, M. Oltean, V. Chis and N. Leopold, *Vib. Spectrosc.*, 2012, **62**, 165–171.

28 V. V. Butova, O. A. Burachevskaya, M. A. Muratidi, I. I. Surzhikova, P. V. Zolotukhin, P. V. Medvedev, I. E. Gorban, A. A. Kuzharov and M. A. Soldatov, *Inorg. Chem.*, 2021, **60**, 5694–5703.

29 C. A. Téllez S., E. Hollauer, M. A. Mondragon and V. M. Castaño, *Spectrochim. Acta, Part A*, 2001, **57**, 993–1007.

30 B. Athokpam, S. G. Ramesh and R. H. McKenzie, *Chem. Phys.*, 2017, **488–489**, 43–54.

31 S. A. Ravichandran, V. P. Rajan, P. V. Aravind, A. Seenivasan, D. G. Prakash and K. Ramakrishnan, *Macromol. Symp.*, 2016, **361**, 30–33.

32 A. M. A. El-Hamid, M. A. Zahran, Y. M. Z. Ahmed and S. M. El-Sheikh, *Radiochemistry*, 2020, **62**, 243–250.

33 Y. Luan, M. Yang, Q. Ma, Y. Qi, H. Gao, Z. Wu and G. Wang, *J. Mater. Chem. A*, 2016, **4**, 7641–7649.

34 S. S. Musbah, V. Radojević, I. Radović, P. S. Uskoković, D. B. Stojanović, M. Dramićanin and R. Aleksić, *J. Min. Metall., Sect. B*, 2012, **48**, 309–318.

35 F. C. Bononi, Z. Chen, D. Rocca, O. Andreussi, T. Hullar, C. Anastasio and D. Donadio, *J. Phys. Chem. A*, 2020, **124**, 9288–9298.

36 S. Zhang, Y. Cheng, W. Xu, J. Li, J. Sun, J. Wang, C. Qin and L. Dai, *RSC Adv.*, 2017, **7**, 56682–56690.

37 M. Nilsson, I. F. Duarte, C. Almeida, I. Delgadillo, B. J. Goodfellow, A. M. Gil and G. A. Morris, *J. Agric. Food Chem.*, 2004, **52**, 3736–3743.

38 R. J. Abraham, L. Griffiths and M. Perez, *Magn. Reson. Chem.*, 2014, **52**, 395–408.

39 M. Giyahchi and H. Moghimi, *Sci. Rep.*, 2023, **13**, 1–10.

40 M. G. Mohamed, C. H. Hsiao, F. Luo, L. Dai and S. W. Kuo, *RSC Adv.*, 2015, **5**, 45201–45212.

41 S. Bennabi and M. Belbachir, *J. Inorg. Organomet. Polym. Mater.*, 2017, **27**, 1787–1799.

42 J. Wang, J. Wang, S. Zuo, J. Pei, W. Liu and J. Wang, *Chin. Chem. Lett.*, 2023, **34**, 108157.

43 D. Kim, Y. H. Jin, K. W. Jeon, S. Kim, S. J. Kim, O. H. Han, D. K. Seo and J. C. Park, *RSC Adv.*, 2015, **5**, 74790–74801.

44 J. Mao, H. Fan, S. Lian, G. I. N. Waterhouse and S. Ai, *Appl. Phys. A:Mater. Sci. Process.*, 2019, **125**, 419.

45 N. Sinha and O. S. Wenger, *J. Am. Chem. Soc.*, 2023, **145**, 4903–4920.

46 T. Hamada, K. Manabe, S. Ishikawa, S. Nagayama, M. Shiro and S. Kobayashi, *J. Am. Chem. Soc.*, 2003, **125**, 2989–2996.

47 X. Hu, K. Ma, A. Sabbaghi, X. Chen, A. Chatterjee and F. L. Y. Lam, *Mol. Catal.*, 2020, **482**, 110635.

48 C. Tian, L. Zhu, F. Lin and S. G. Boyes, *ACS Appl. Mater. Interfaces*, 2015, **7**, 17765–17775.

49 N. V. Klassen, V. V. Kedrov, Y. A. Ossipyan, S. Z. Shmurak, I. M. Shmytńko, O. A. Krivko, E. A. Kudrenko, V. N. Kurlov, N. P. Kobelev, A. P. Kiselev and S. I. Bozhko, *IEEE Trans. NanoBiosci.*, 2009, **8**, 20–32.

50 S. Tajahmadi, A. Shamloo, A. Shojaei and M. Sharifzadeh, *ACS Omega*, 2022, **7**, 41177–41188.

51 P. A. Demakov, A. A. Vasileva, V. A. Lazarenko, A. A. Ryadun and V. P. Fedin, *Crystals*, 2021, **11**, 1375.

52 M. Naderi, *Prog. Filtr. Sep.*, 2015, 585–608.

53 I. Nongwe, V. Ravat, R. Meijboom and N. J. Coville, *Appl. Catal., A*, 2016, **517**, 30–38.

54 L. Xu, J. Zhang, J. Ding, T. Liu, G. Shi, X. Li, W. Dang, Y. Cheng and R. Guo, *Minerals*, 2020, **10**(1), 72.

55 M. A. Hamouda, S. M. Sheta, R. R. Sheha, A. T. Kandil, O. I. Ali and S. M. El-Sheikh, *RSC Adv.*, 2022, **12**, 13103–13110.

56 M. A. Attia, S. I. Moussa, R. R. Sheha, H. H. Someda and E. A. Saad, *Appl. Radiat. Isot.*, 2019, **145**, 85–94.

57 R. R. Sheha and E. A. El-Shazly, *Chem. Eng. J.*, 2010, **160**, 63–71.

58 L. Khezami, K. K. Taha, E. Amami, I. Ghiloufi and L. El Mir, *Desalin. Water Treat.*, 2017, **62**, 346–354.

59 F. A. Cotton, G. Wilkinson, C. A. Murillo and M. Bochmann, *Advanced Inorganic Chemistry*, John Wiley & Sons, 1999.

60 M. Eftekhari, M. Gheibi, H. Monhemi, M. Gaskin Tabrizi and M. Akhondi, *Adv. Powder Technol.*, 2022, **33**, 103577.

61 P. Zong, M. Shao, X. Xu, M. Xu, N. Yan, S. Wang, Y. Yang, J. Chen and Z. Qiu, *J. Mol. Liq.*, 2022, **360**, 119565.

62 P. Misaelides, P. Misaelides, P. Misaelides, S. Sarri, S. Sarri, S. Sarri, D. Zamboulis, D. Zamboulis, D. Zamboulis, G. Gallios, G. Gallios, G. Gallios, I. Zhuravlev and V. V. Strelko, *J. Radioanal. Nucl. Chem.*, 2006, **268**, 53–58.

63 S. Lu, X. Song, H. Xu, Q. Liu and M. Wang, *J. Radioanal. Nucl. Chem.*, 2012, **291**, 889–895.

64 S. Iftekhar, V. Srivastava and M. Sillanpää, *Chem. Eng. J.*, 2017, **320**, 151–159.